

Article

Experimental Study and Engineering Application of the Spatial Reticulated Grid Bolt-Shotcrete Support Structure for Excavation Tunnels

Mingli Huang ¹, Yuan Song ^{1,2,*} , Xudong Zhang ³ and Tong Sun ¹

¹ Key Laboratory of Urban Underground Engineering of Ministry of Education, Beijing Jiaotong University, Beijing 100044, China

² School of Civil Engineering and Architecture, Anhui University of Science and Technology, Huainan 232001, China

³ China Railway 11th Bureau Group Co., Ltd., Wuhan 430061, China

* Correspondence: 18115036@bjtu.edu.cn; Tel.: +86-130-8368-9492

Abstract: In view of the problems of rapid construction and deformation control of large cross-section tunnels in complex urban environments, the concept of “timely high-strength support” was put forward to form strong support over time and bear the load of surrounding rock in real time, and innovatively developed the spatial reticulated grid bolt-shotcrete support structure (SRGB). The research in this paper focuses on the supporting principle, bearing mechanical properties, snatch simulation test, construction process, and engineering application effects. The components of the SRGB and their respective functions were expounded in detail. The failure modes and deformation characteristics of the tested components were revealed through the indoor loading test, and the performance characteristics of the spatial reticulated grid concrete components with high strength and high rigidity were displayed. With the help of the multi-functional operation trolley, the assembly process test of the spatial reticulated grid was carried out, which verified the feasibility of mechanized construction and the rationality of structural design. Relying on the underground tunnel project of Guangzhou Metro, the spatial reticulated grid structure was successfully used as the initial support of the tunnel for the first time, forming a complete set of mechanized rapid construction technology for a large cross-section tunnel, and constructing a timely high-strength support system suitable for the complex urban environment. The research results provide a new idea and new technology for the mechanized rapid construction and efficient support of large cross-section tunnels.

Keywords: excavation tunnel; spatial reticulated grid; bolt-shotcrete support; model test; bearing performance; mechanization; field test



Citation: Huang, M.; Song, Y.; Zhang, X.; Sun, T. Experimental Study and Engineering Application of the Spatial Reticulated Grid Bolt-Shotcrete Support Structure for Excavation Tunnels. *Appl. Sci.* **2022**, *12*, 8506. <https://doi.org/10.3390/app12178506>

Academic Editors: Mingfeng Lei, Chenjie Gong and Xianda Shen

Received: 3 July 2022

Accepted: 23 August 2022

Published: 25 August 2022

Publisher's Note: MDPI stays neutral with regard to jurisdictional claims in published maps and institutional affiliations.



Copyright: © 2022 by the authors. Licensee MDPI, Basel, Switzerland. This article is an open access article distributed under the terms and conditions of the Creative Commons Attribution (CC BY) license (<https://creativecommons.org/licenses/by/4.0/>).

1. Introduction

Since the beginning of the 21st century, the number and the scale of tunnels and underground projects in China have achieved unprecedented development, and the engineering construction conditions and geological environment have become more and more complex. In particular, the large-scale urban underground traffic construction has brought many new challenges to construction safety and operation safety, and has become a scientific problem that needs to be solved urgently in the construction of underground projects. Some scholars pointed out that the safety assessment of tunnel stability is crucial to tunnel construction, and accurate analysis can lead to reliable predictions [1–4]. Under the guidance of the NATM theory, China has formed a variety of tunnel support concepts and technologies. In general, the tunnel support method has gradually changed from single support to combined support. The support concept has also changed from emphasizing the role of secondary lining support to paying attention to the primary support to bear the load of surrounding rock, and the secondary lining is only used as a safety reserve.

The combined support type composed of a grid arch, anchor bolt, and shotcrete is a widely used flexible support type, which can maximize the self-bearing capacity of the surrounding rock and allow appropriate deformation of the surrounding rock. Many scholars at home and abroad have carried out in-depth research on the bearing mechanism and support performance of grid arches, and have reported a series of achievements. Baumann and Betzle [5] took the lead in designing a three-limb grid arch, and verified the rationality of the structural design, combined with field application tests. Nomikos et al. [6] conducted an in-depth analysis of the mechanical characteristics of the three-limb grid arch, and expounded the mechanical response under different parameters. Kim et al. [7] analyzed the differences in ultimate bearing capacity and structural stability between the new four-limb grid arch and the three-limb grid arch through indoor tests and numerical simulations. Lee et al. [8] carried out research on the mechanical properties of a high-strength grid arch, obtained reasonable structural design parameters, and the good stability and bearing performance of this structure are verified. Kim et al. [9] presented an evaluation of the structural performance of tetragonal lattice girders for NATM tunnel construction, and evaluated the ultimate carrying capacity and checked the rationality of the connection method of the girder. Qiu et al. [10] evaluated the relationship between the ultimate bearing capacity of a four-limb grid arch and its component cost, and systematically studied the influence of factors such as web bar diameter and weld length on the mechanical properties of the grid arch. Tan and Han [11] carried out a field test of heat-treated high-strength lattice girders in railway tunnels and highway tunnels, compared the support performance with the original-design I20b steel arch, and achieved good application results. Gong et al. [12] and Ding et al. [13] studied the mechanical properties of concrete segment joints of different materials in shield tunnels, verified the design method, and conducted in-depth research on the waterproof performance of different joints.

Rigid support structures are usually used to bear strong loose ground pressure, such as concrete-filled steel tubulars [14], prefabricated arc plates [15], spatial reticulated grids [16,17], high-strength shotcrete [18], high-strength pre-stressed anchors [19], pretensioned bolt-cable cooperative support [20], etc. It is highly necessary to control the deformation of the deep weak surrounding rock by erecting a supporting structure with high rigidity and high strength. After the excavation of the tunnel, high support strength is applied to the surrounding rock, so that the support object and the surrounding rock within a certain range around the tunnel can work together to improve the bearing capacity of the deep rock mass, preventing the development of rheological failure to ensure long-term stability.

However, in the construction of some high-energy geological environment tunnels, it is not appropriate to adopt the traditional strengthened support [21]. One should gradually release the surrounding rock pressure under certain constraints, allowing large deformation of the surrounding rock and support, and finally achieving a balance between the two. By focusing on the structural characteristics of the support structure, the steel frame can adaptively adjust the deformation of the surrounding rock and release the excess energy accumulated by the support object. The surrounding rock pressure can be released through energy-consuming devices or other measures, allowing large deformation of the surrounding rock and supporting structure, and can provide sufficient supporting resistance to prevent lining cracking, twisting or even breaking of steel arches. In order to realize the effective support of soft rock tunnels, many scholars have also proposed a series of support theories and technical support systems, such as resistance-limiting and energy-dissipating support [22–24], prefabricated arc plate of reinforced concrete [25], stone masonry secondary support [26], concrete-filled steel tubular bolt-shotcrete support [27,28], a π -type steel-concrete composite structure [29], steel grid-concrete core tube [30], semi-rigid wire-shell bolting shotcrete [31,32] and other support forms.

Based on the above analysis of the current situation of tunnel (roadway) support technologies, the research on the use of the spatial reticulated grid is still rarely involved in the tunnel engineering field, and there is a lack of necessary discussion on the mechanism and mechanical characteristics of the SRGB structure. Therefore, this paper designs a high-strength

and high-rigidity initial tunnel support structure based on the current situation of the construction of shallow-buried large-section tunnels in complex urban environments, which involve difficult construction processes, high safety risks, and tight construction schedules. The bearing characteristics and failure mechanism are analyzed through indoor model tests, and industrial tests are carried out, relying on the Guangzhou subway tunnel project to provide a reasonable new support type for urban shallow-buried large-section tunnels.

2. The Principle of the SRGB Support Structure

The SRGB support structure is composed of a systematic bolt, shotcrete and spatial reticulated grid, as shown in Figure 1. Among them, the systematic bolt and shotcrete belong to the category of flexible support, allowing moderate deformation of surrounding rock. As a new supporting structure, the spatial reticulated grid is based on high-strength seamless steel tubes as the main force-bearing parts, and threaded steel bars as the connecting webs. The full-section enclosed support structure, connected by bolted end-plates, adopts the continuous erection method, showing the stress characteristics of surface bearing.

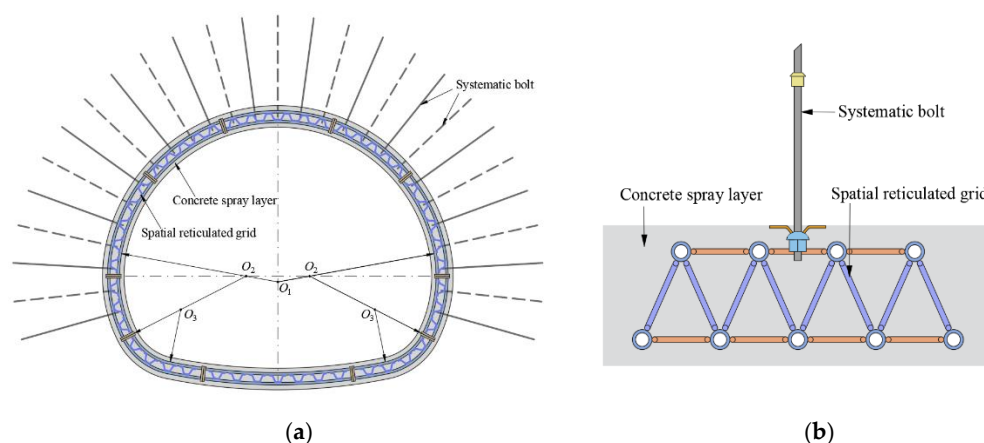


Figure 1. The SRGB support structure. (a) The components of the support system and (b) sectional structure feature.

The SRGB support structure takes into account the characteristics of flexible support and rigid support. It gives full play to the advantages of the bolt and shotcrete, and the bolt anchored into the rock mass is integrated with the surrounding rock, so as to improve the stress state and the stability of the surrounding rock. After the tunnel is excavated, the surrounding rock should be sealed by spraying concrete over time, so that the surrounding rock is in a state of three-way stress, forming a combined structure to coordinately bear the load. The spatial reticulated grid draws on the structural form of the large-span grid structure on the ground, and combines the implementation environment of tunnels and underground projects to make a special support structure. This structure has the characteristics of high rigidity, high strength and good stability, and can be used to bear strong loosening pressure. The above-mentioned systematic bolt, spray layer and spatial reticulated grid together constitute the initial support system. The bolt shotcrete support is applied over time in the early stage, which has the effect of quickly sealing the surrounding rock and improving the stress state of the surrounding rock, and then erecting the high-strength arches and re-spraying concrete are carried out to form a permanent lining structure. This structure gives full play to the performance advantages of high-strength steel tubes and concrete materials, and reflects the support concept that the initial support should form strong support in time and bear the surrounding rock pressure in real time.

In tunnel engineering, the support scheme should be reasonably determined according to the different surrounding rock conditions and surrounding environment. For the challenge of strict deformation control in urban complex environment areas, the characteristics of coordinated deformation of bolt shotcrete flexible support and surrounding rock should

be brought into play, and the basic load of the surrounding rock could be borne in real time, with the help of a high-strength and high-rigidity spatial reticulated grid structure to meet the bearing capacity and stability requirements of the tunnel.

3. Indoor Tests of the Spatial Reticulated Grid Concrete Components

In order to grasp the synergistic effect of the spatial reticulated grid and shotcrete, the laboratory tests under a pure bending load were carried out for the end-plate joint concrete component and jointless concrete component, the failure mode and stress characteristics of the components were analyzed, and the influence mechanism of the joint structure on the bearing performance of the support structure was also clarified.

3.1. Component Design and Production

3.1.1. Component Design

The tested components include the bolted end-plate joint concrete component (BEJC50 × 6) and the jointless concrete component (JSC50 × 6). The size of the components (length × width × height) is 3200 mm × 1200 mm × 350 mm, and the thickness of upper and lower protective layers is 40 mm. The shotcrete is made of commercial concrete with a strength grade of C25. Combined with the data provided by the laboratory test and the concrete manufacturer, it is concluded that the elastic modulus of the concrete is 26.2 GPa, and the compressive strength is 27.5 MPa. The main structural parameters of the tested components are shown in Table 1. In the components, the main limb steel tube is Q420 high-strength seamless steel, with the diameter of 50 mm and the wall thickness of 6 mm, and the steel tube spacing is 200 mm. π-shaped and U-shaped bars adopt HRB400 threaded bars with the diameter of 14 mm. The end-plate is made of Q235B carbon structural steel, with the thickness of 20 mm. The properties of the steel materials are shown in Table 2. The schematic diagram of spatial reticulated grid concrete components is shown in Figure 2.

Table 1. Main structural parameters of the tested components.

Component Type	Length (mm)	Width (mm)	Height (mm)	Concrete Grade	Steel Tube Size (mm)	End-Plate Thickness (mm)	π-Shaped or U-Shaped Rebar Diameter (mm)	Bolt Size
BEJC50 × 6 component	3200	1200	350	C25	50 × 6	20	14	M24
JSC50 × 6 component	3200	1200	350	C25	50 × 6		14	

Table 2. Mechanical properties of the steel materials.

Material	Elastic Modulus (GPa)	Yield Strength (MPa)	Ultimate Tensile Strength (MPa)	Elongation Ratio (%)
14 mm reinforcement	198	430.34	576.81	23.60
20 mm thickness steel plate	205	254.62	427.25	24.58
50 × 6 mm steel tube	205	457.78	604.61	25.47

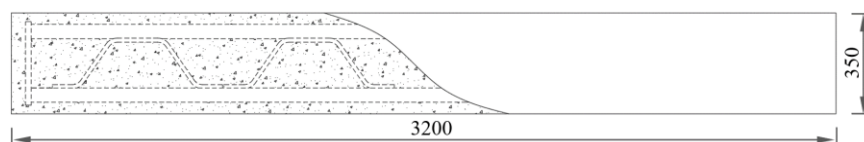


Figure 2. The schematic diagram of spatial reticulated grid concrete components.

3.1.2. Component Production

According to the size of the components, the appropriate pouring formwork is made, and concrete pouring, vibration, troweling, curing and other processes are carried out in

the laboratory to ensure suitable curing conditions and effective curing quality control. The specific production process of the components is shown in Figures 3 and 4.

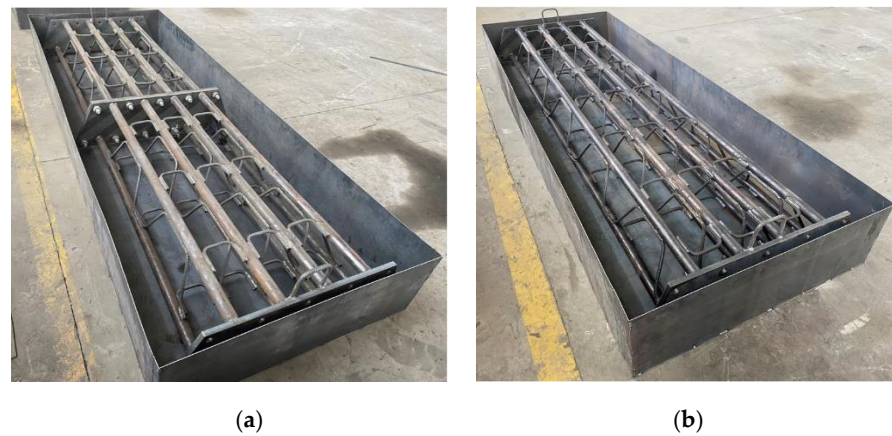


Figure 3. Before pouring of the spatial reticulated grid components. (a) The bolted end-plate joint component and (b) the jointless component.

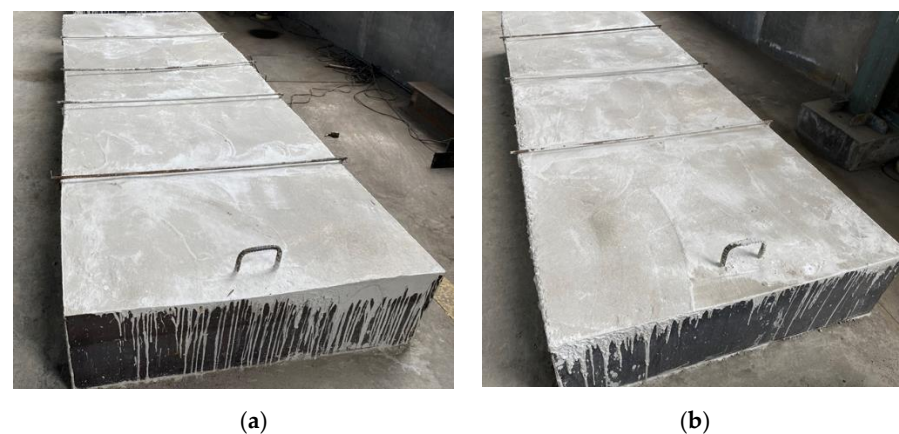


Figure 4. After pouring of the spatial reticulated grid components. (a) The BEJC50 \times 6 component and (b) the JSC50 \times 6 component.

3.2. Test Loading and Measurement

The pure bending loading tests were carried out on the Y32-500A four-column hydraulic servo loading system. The two vertical actuators can provide a load pressure with a maximum nominal force of 5000 kN. The four-point loading mode is adopted to ensure that the components are in the pure bending state. The loading is carried out in the following three steps: first, one must preload the components to ensure good contact between the components and the loading device; then, the monotonic step-by-step loading method is adopted, and the load increment of each level is 20 kN; when the load pressure is no longer increased, the displacement loading method is changed until the component is damaged and unstable. The load pressure, mid-span deflection, concrete strain and other data are collected in real time through the JMZX-3006 comprehensive tester and the YBCS-CH60 high-speed static strain test and analysis system. The actual indoor loading is shown in Figure 5.

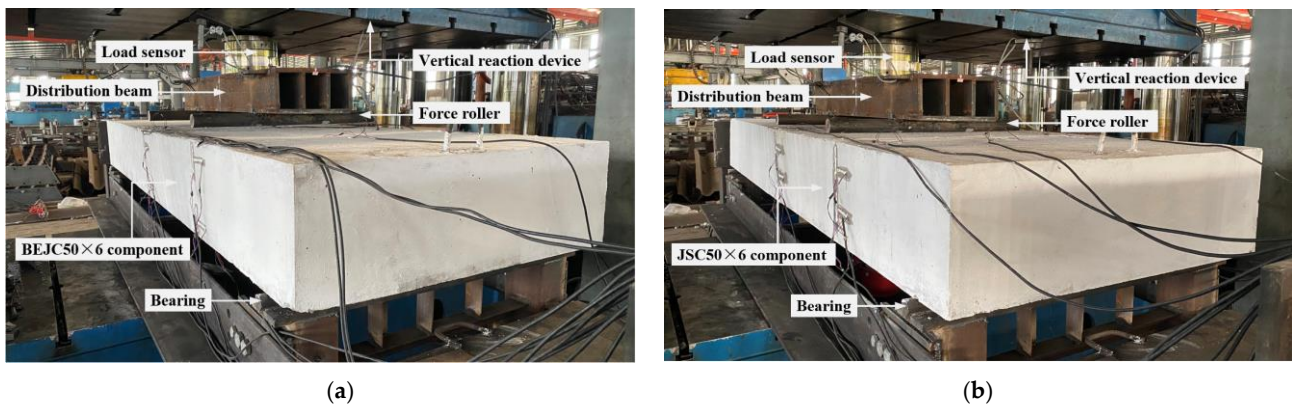


Figure 5. Indoor loading tests. (a) The BEJC50 × 6 component and (b) the JSC50 × 6 component.

By considering the cracking failure of concrete and the bending deformation of components, two concrete strain monitoring sections were arranged at the mid-span and quarter point positions, six sets of strain gauges (vertical and horizontal) were pasted on the top and bottom surfaces, and four sets of strain gauges (vertical and horizontal) were pasted on the front and back surfaces. Two digital displacement meters were installed at the midspan position to monitor the deflection of the component during the loading process. The specific arrangement of strain measuring points is shown in Figure 6.

Top	CS-1	CS-2	CS-1	CS-2
	CS-3	CS-4	CS-3	CS-4
	CS-5	CS-6	CS-5	CS-6
Back	CS-7	CS-8	CS-7	CS-8
	CS-9	CS-10	CS-9	CS-10
Bottom	CS-11	CS-12	CS-11	CS-12
	CS-13	CS-14	CS-13	CS-14
	CS-15	CS-16	CS-15	CS-16
Front	CS-17	CS-18	CS-17	CS-18
	CS-19	CS-20	CS-19	CS-20

Figure 6. The arrangement of strain measuring points.

3.3. Test Results and Analysis

3.3.1. Experimental Phenomena

(1) The BEJC50 × 6 component

As shown in Figure 7, under the action of the pure bending load, small vertical cracks are generated on the tensile side of the mid-span of the BEJC50 × 6 component, and the cracks continue to expand upward with the continuous application of the load. At the same time, the crack width also increases continuously. When the load increases to a certain extent, the number of vertical cracks increases, and oblique cracks appear. There is a certain regularity in the appearance of the overall cracks, the concrete sprayed layer has good adhesion with the spatial reticulated grid, and no concrete fragments fall off.



Figure 7. Failure characteristics of the BEJC50 × 6 component.

(2) The JSC50 × 6 component

As shown in Figure 8, during the loading process, a number of vertical cracks occurred on the tensile side of the pure bending section of the JSC50 × 6 component in the middle span. With the continuous increase in the load, the cracks continue to grow upward and generate oblique cracks. When the loading reaches a certain level, small oblique cracks begin to appear between the support and the pure bending section. With the continuous application of the load, the length and width of the cracks gradually increase. The appearance of the overall cracks of the component also has a certain regularity, and the component is unstable and damaged, due to the cracking and crushing of the concrete spray layer at the end of loading.

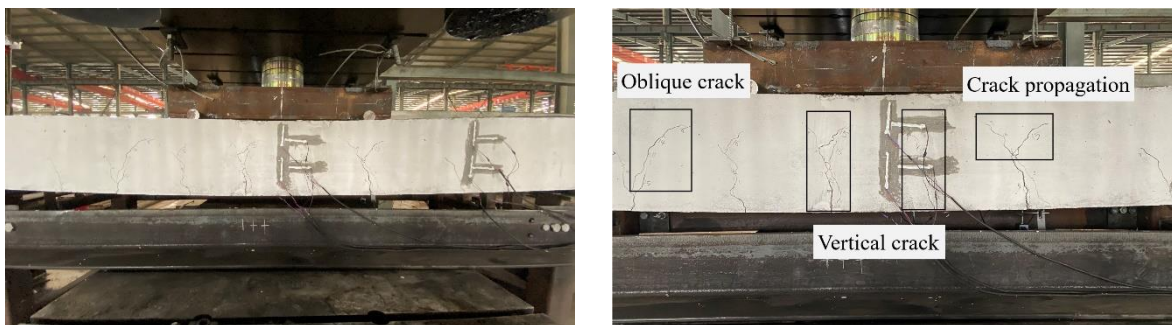


Figure 8. Failure characteristics of the JSC50 × 6 component.

3.3.2. Deflection Displacement

(1) The BEJC50 × 6 component

Figure 9 shows the relationship between the mid-span deflection displacement and the bending moment of the BEJC50 × 6 component under the pure bending loading. Combined with the experimental phenomenon, it can be observed that the overall deformation process of the component is divided into the following three stages: elastic deformation stage, failure stage, and strength degradation stage. In the initial stage of loading, the bending moment of the component is small, the change rate of deflection displacement is stable, and it simply increases linearly with the load. At this time, it is in the elastic deformation stage. The bending moment continues to be applied, the deflection growth rate gradually increases, and the concrete cracks continue to expand. When the ultimate bearing capacity is reached, the bending moment value of the component suddenly drops sharply, and the component has been damaged. The load continues to be loaded, the bearing capacity of the component gradually decreases, and the deflection changes sharply. This phase is called the strength degradation stage. The maximum bending moment of the component when it reaches the ultimate load-bearing state is 324.5 kN·m, and the mid-span deflection is about

12.0 mm. The loading process is always accompanied by the occurrence and expansion of cracks and the deterioration of bearing performance.

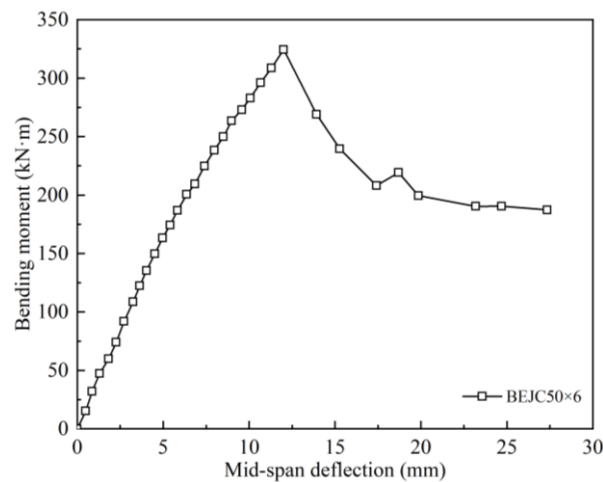


Figure 9. The bending moment–midspan deflection curve of the BEJC50 × 6 component.

(2) The JSC50 × 6 component

Figure 10 shows the relationship between the mid-span deflection displacement and the bending moment of the JSC50 × 6 component under the pure bending loading. Combined with the experimental phenomenon, it can be observed that the overall deformation process can be divided into the following three stages: elastic deformation stage, plastic deformation stage, and failure stage. When the bending moment is small, the deflection displacement increases linearly with the load. When the bending moment increases to a certain level, the bearing capacity remains relatively stable. At this stage, multiple vertical cracks and derivative cracks with uniform intervals appear on the whole component. After approaching the ultimate bearing state, the deflection growth rate is significantly accelerated, and the bending moment value of the component drops significantly, indicating that the component has been damaged. The ultimate bearing capacity of the JSC50 × 6 component is 378.8 kN·m, and the mid-span deflection is about 50.1 mm. Compared with the BEJC50 × 6 component, the allowable deformation and bearing capacity of the JSC50 × 6 component is higher, but the bending stiffness is slightly lower.

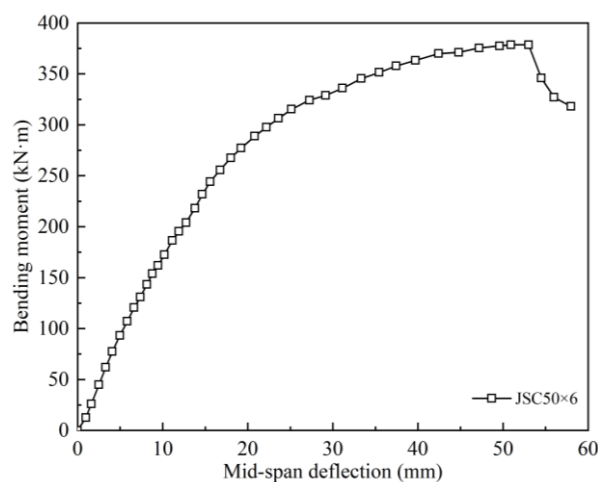


Figure 10. The bending moment–midspan deflection curve of the JSC50 × 6 component.

3.3.3. Concrete Strain

(1) The BEJC50 × 6 component

The relationship curves of the concrete surface strain and bending moment of the BEJC50 × 6 component are shown in Figures 11 and 12, including two monitoring sections at the 1/2 and 1/4 positions.

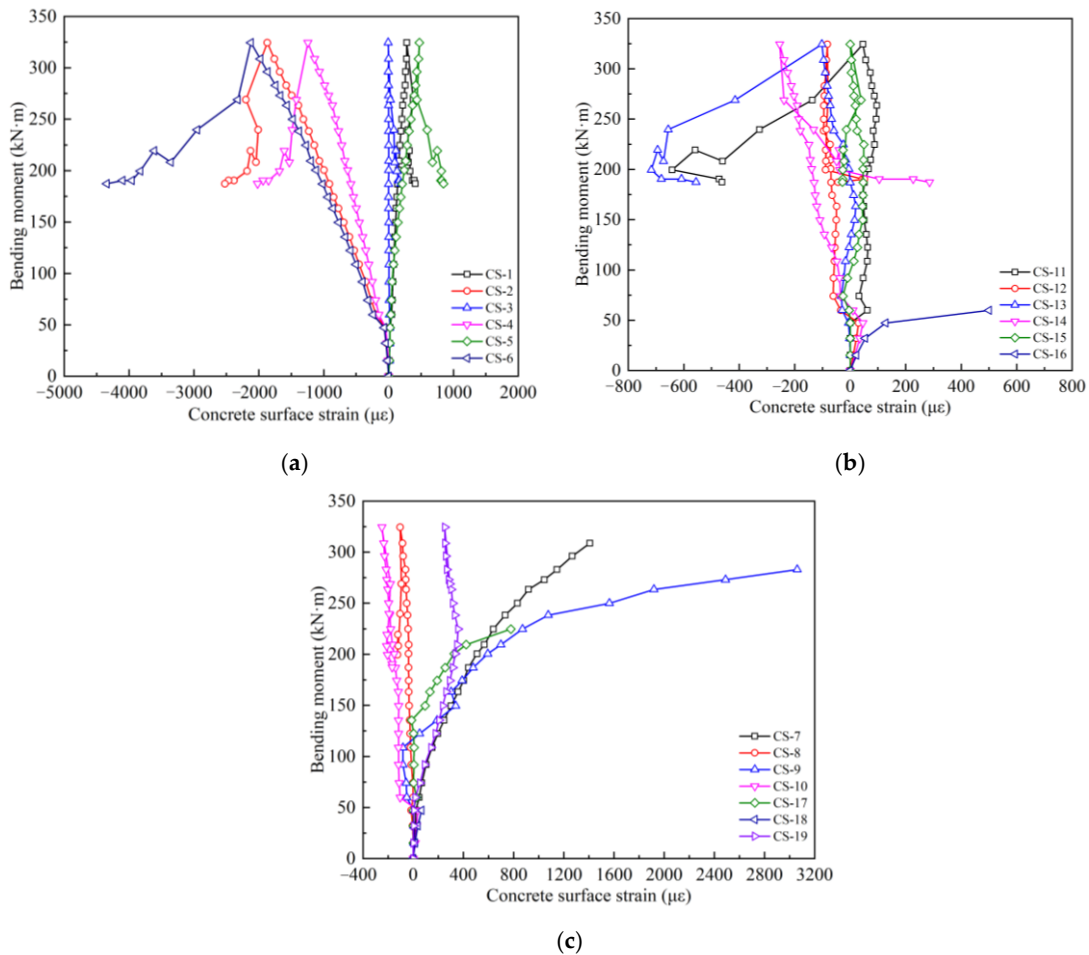


Figure 11. The bending moment–concrete strain relationship curves of 1/2 section: (a) monitoring points on top surface, (b) monitoring points on the bottom surface, (c) monitoring points on front and back surfaces.

From the Figure 11, it can be observed that the measuring points CS-1, CS-3, and CS-5 on the upper surface of the component are in the tension state, the maximum tensile strain occurs at the measuring point CS-5, which is $474 \mu\epsilon$, and the corresponding stress value is about 10.9 MPa, which is far greater than the ultimate tensile strength of the concrete. The measuring points CS-2, CS-4, and CS-6 show an obvious compressive state. The maximum compressive strain occurs at the measuring point CS-6, which is $-2122 \mu\epsilon$, and the corresponding stress value is about 48.8 MPa, which has exceeded the ultimate compressive strength of the concrete. The measuring points on the lower surface of the component show a certain degree of tension state at the initial stage of loading, and then change to the compressive state. The maximum tensile and compressive strains occur at the measuring points CS-11 and CS-14, which are $46 \mu\epsilon$ and $-254 \mu\epsilon$ respectively. In the front and back surfaces of the component, the measuring points CS-7, CS-9, CS-17, and CS-19 show an obvious tension state, and the maximum strain of the measuring point CS-9 reaches $3061 \mu\epsilon$, which has exceeded the ultimate strength of the concrete. The measuring points CS-8, CS-10, and CS-18 exhibit a compressive state, and the maximum compressive

strain occurred at the measuring point CS-10, which is $-250 \mu\epsilon$, and the stress value is about 5.75 MPa.

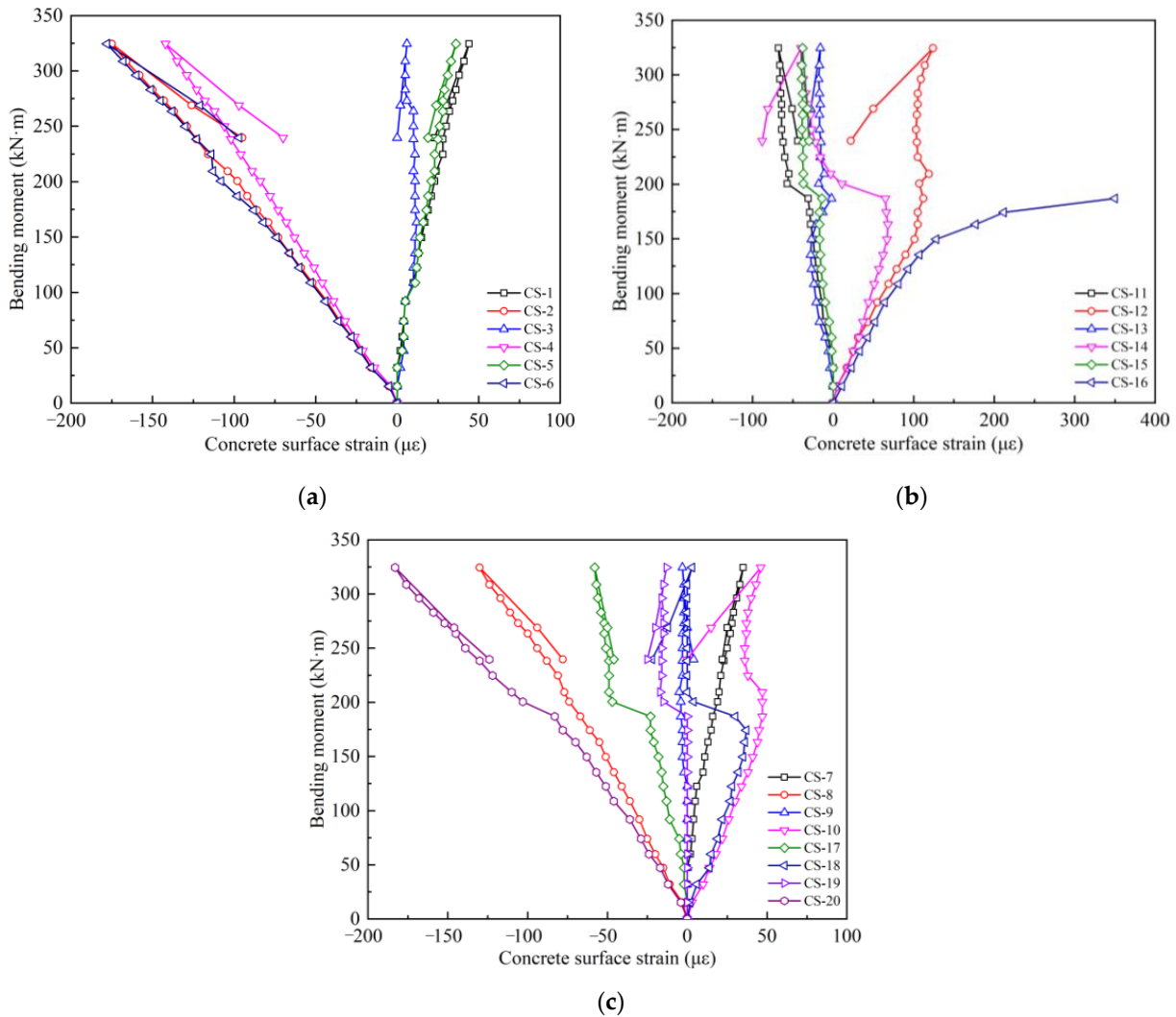


Figure 12. The bending moment–concrete strain relationship curves of 1/4 section: (a) monitoring points on top surface, (b) monitoring points on the bottom surface, (c) monitoring points on front and back surfaces.

From the Figure 12, it can be observed that the measuring points CS-1, CS-3, and CS-5 on the upper surface show a certain degree of the tension state, and the maximum tensile strain occurs at the measuring point CS-1 when the component is fails, and the strain is $44 \mu\epsilon$. The measuring points CS-2, CS-4 and CS-6 are in the compression state, the maximum compressive strain occurs at the measuring point CS-6, which is $-178 \mu\epsilon$, and the stress value is about 4.1 MPa. The measuring points CS-11, CS-13, and CS-15 on the lower surface show a certain degree of the compression state. The maximum compressive strain occurs at the measuring point CS-11, which is $-68 \mu\epsilon$, and the stress value is about 1.56 MPa. The measuring points CS-12, CS-14, and CS-16 show an obvious tensile state, and the maximum tensile strain occurs at the measuring point CS-16, which is $350 \mu\epsilon$, and the stress value is about 8.05 MPa, which has exceeded the ultimate tensile strength of the concrete. The measuring points CS-7, CS-10, and CS-18 on the front and back surfaces are in the tension state, the maximum tensile strain occurs at the measuring point CS-10, which is $46 \mu\epsilon$, and the stress value is about 1.1 MPa. The measuring points CS-8, CS-17, CS-19,

and CS-20 are in the compression state. The maximum compressive strain occurs at the measuring point CS-20, which is $-183 \mu\epsilon$, and the stress value is about 4.2 MPa.

(2) The JSC50 \times 6 component

The relationship curves of the concrete surface strain and bending moment of the JSC50 \times 6 component are shown in Figures 13 and 14, including two monitoring sections at the 1/2 and 1/4 positions.

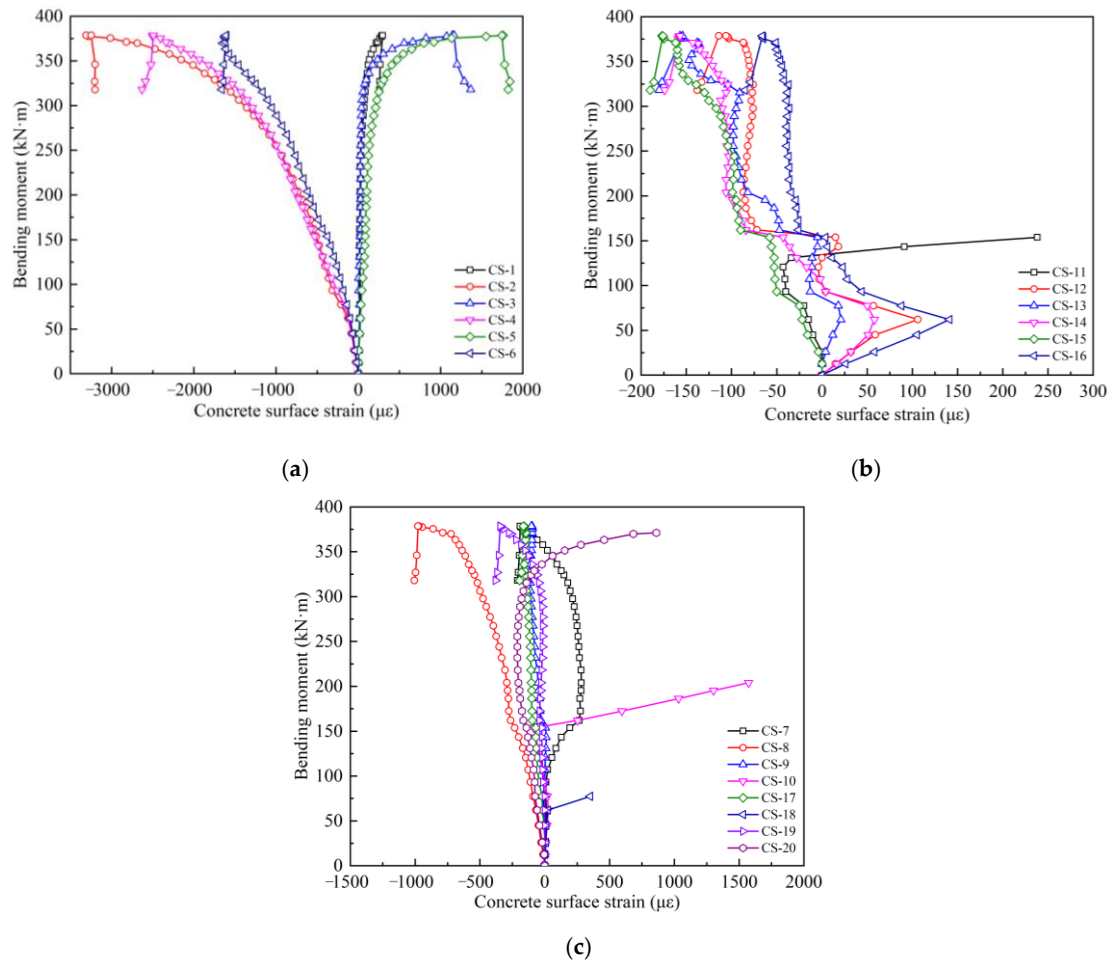


Figure 13. The bending moment–concrete strain relationship curves of 1/2 section: (a) monitoring points on top surface, (b) monitoring points on the bottom surface, (c) monitoring points on front and back surfaces.

From the Figure 13, it can be observed that the strain of each measuring point on the upper surface grows smoothly during the whole loading process. The measuring points CS-1, CS-3, and CS-5 are in the tension state, and the maximum tensile strain occurs at the measuring point CS-5, which is $1728 \mu\epsilon$, and the stress value is about 39.7 MPa, which is much larger than the ultimate tensile strength of concrete. The measuring points CS-2, CS-4, and CS-6 are in the compressive state. The maximum compressive strain occurs at the measuring point CS-2, which is $-3316 \mu\epsilon$, and the stress value is about 76.3 MPa, which has exceeded the ultimate compressive strength of the concrete. For each measuring point on the lower surface, the strain grows rapidly at the initial stage of loading, and then the strain shows a regular “step” jump, which is related to the regular generation and expansion of concrete cracks. In the later stage, the growth rate of concrete strain is relatively slow. The maximum compressive strain occurs at the measuring point CS-15, which is $-177 \mu\epsilon$, and the stress value is about 4.1 MPa. The measuring points CS-7, CS-10, CS-18, and CS-20 on the front and back surfaces are in the tensile state, and the maximum

strain of the measuring point CS-10 reaches $1792 \mu\epsilon$, and the stress value is about 41.2 MPa. The measuring points CS-8, CS-9, CS-17, and CS-19 are in the compressive state, and the maximum compressive strain occurred at the measuring point CS-8, which is $-969 \mu\epsilon$, and the stress value is about 22.3 MPa.

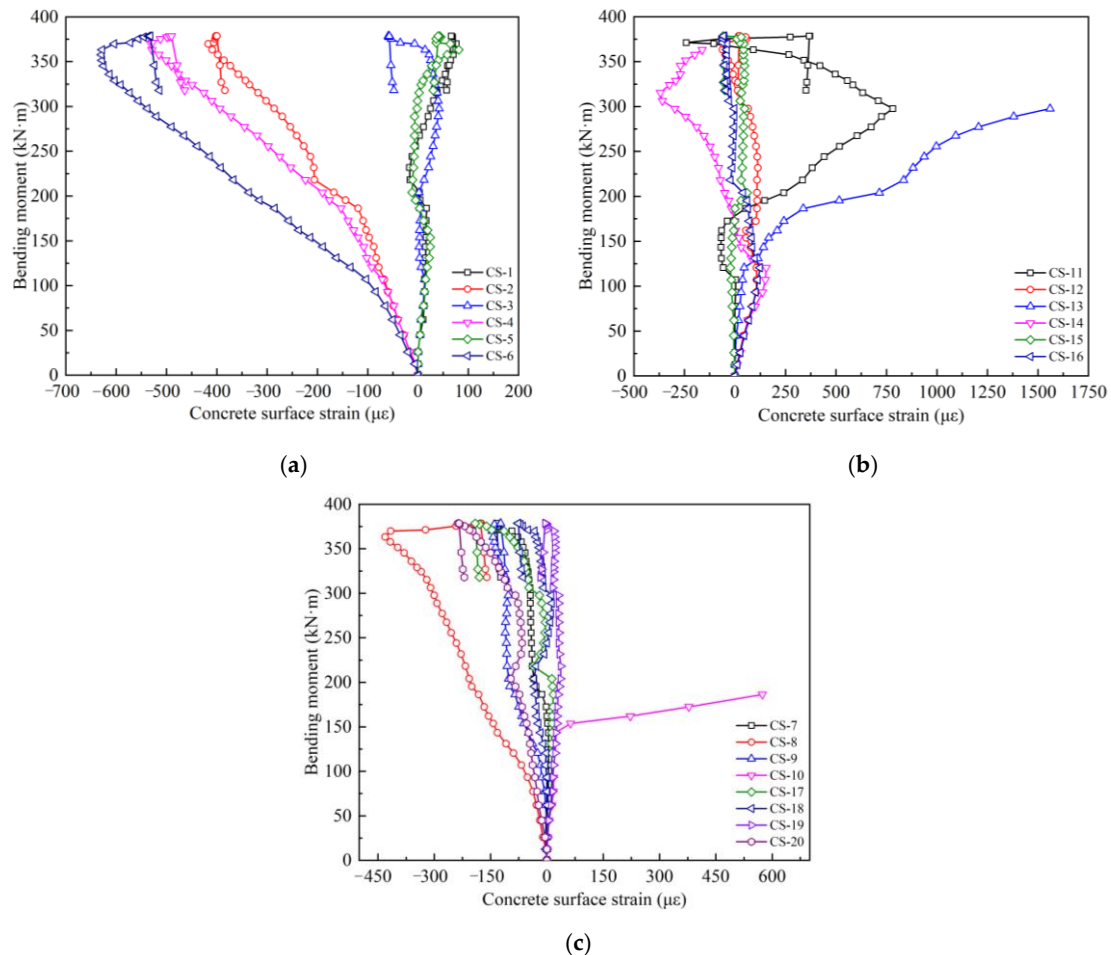


Figure 14. The bending moment–concrete strain relationship curves of 1/4 section: (a) monitoring points on top surface, (b) monitoring points on the bottom surface, (c) monitoring points on front and back surfaces.

From the Figure 14, it can be observed that the upper surface measuring points CS-1, CS-3, and CS-5 are in the tension state, the maximum tensile strain occurs at the measuring point CS-5, which is $81 \mu\epsilon$, and the stress value is about 1.9 MPa. The measuring points CS-2, CS-4, and CS-6 are evidently in the compression state, the maximum compressive strain occurs at the measuring point CS-6, which is $-628 \mu\epsilon$, and the stress value is about 14.4 MPa. The measuring points CS-11, CS-13, and CS-15 on the lower surface are in the tension state, and the maximum strain of the measuring point CS-13 reaches $1560 \mu\epsilon$, which exceeds the ultimate tensile strength of the concrete. The measuring points CS-12, CS-14, and CS-16 are under compression. The maximum compressive strain occurs at the measuring point CS-14, which is $-369 \mu\epsilon$, and the stress value is about 8.5 MPa. The measuring points CS-10 and CS-19 on the front and back surfaces are in the tension state, and the maximum strain of the measuring point CS-10 reaches $574 \mu\epsilon$, and the stress value is about 13.2 MPa, which exceeds the ultimate tensile strength of concrete; the maximum compression strain occurs at the measuring point CS-8, which is $-433 \mu\epsilon$, and the stress value is about 10.0 MPa.

4. Simulation Analysis of the Spatial Reticulated Grid Structure Segmentation and Snatch Assembly

4.1. Determination of the Joint Position of the Spatial Reticulated Grid

Combined with the underground excavation tunnel project between Hengli and Panyu Square Station of Guangzhou Metro Line 22, research on the subsection scheme of the spatial reticulated grid support structure is carried out. The tunnel passes through moderately weathered granite, the surrounding rock is grade IV, the bulk density is $25,000 \text{ N/m}^3$, the elastic modulus is $5 \times 10^3 \text{ MPa}$, Poisson's ratio is 0.2, the cohesion force is 400 kPa, and the internal friction angle is 35° . The burial depth is 26.5 m, the excavation section span is 14.9 m, the height is 11.95 m, and the spray layer thickness is 0.35 m.

The general finite element software ANSYS is used as the calculation tool to analyze the mechanical characteristics of the tunnel support structure by the load-structure method. According to the "Code for Design of Railway Tunnel" [33], the vertical and horizontal uniform force of the surrounding rock are calculated, and then the equivalent nodal force of each node is obtained, and the formation spring is used to simulate the interaction between the surrounding rock and the structure.

The Link10 element and the Beam3 beam element are used to simulate the interaction between the surrounding rock and the structure, and the lining support structure. A gravity load ($g = 9.8 \text{ m/s}^2$) is added to the finite element model through the ANSYS program, the tunnel lining weight is $24,500 \text{ N/m}^3$, Poisson's ratio is 0.28, and the elastic resistance coefficient is 600 MPa/m.

Figure 15 is the internal force distribution diagram of the simulated support structure. From the bending moment diagram, some positions with zero bending moment in the support plane can be obtained. According to this, the joint position of the prefabricated support structure can be preliminarily set at the zero moment.

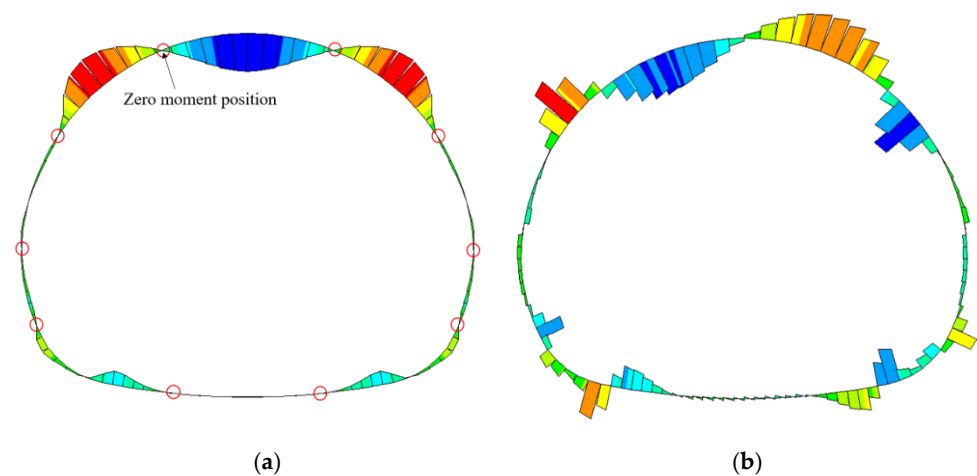


Figure 15. Internal force diagram of primary support structure. (a) Bending moment diagram and (b) shear force diagram.

Combined with the on-site construction method and the load characteristics of the surrounding rock, and taking into account the weight of the components, construction convenience and other factors, the spatial reticulated grid segmentation is systematically analyzed. Each ring of the arch is divided into 10 segments, and the specific joint division is shown in Figure 16a. The height of the upper and lower benches is 7.3 m and 4.65 m, respectively, and the components are divided into five types. The upper bench includes A and B components, and the lower bench includes C, D, and E components. Figure 16b shows the circumferential and longitudinal joint connection types of the spatial reticulated grid. Circumferential joints are connected by the end-plates and high-strength bolts of two adjacent components, and two different U-shaped bolts are used for longitudinal

connections to be placed in the reserved holes, respectively. These connection types are easy to install and operate, and reduce the welding workload to a certain extent.

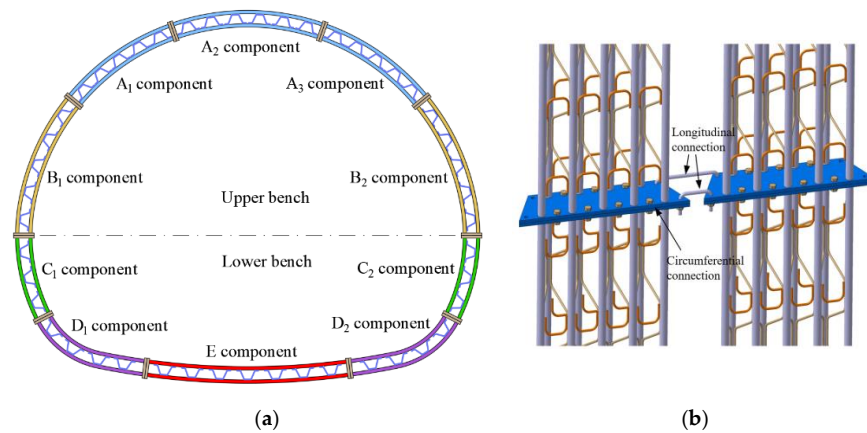


Figure 16. Division scheme and joint connection of the spatial reticulated grid structure. (a) Arch joint distribution and (b) joint connection types.

4.2. Simulation Analysis of Deformation and Force in the Snatch Process of the Spatial Reticulated Grid

Due to the heavy weight of the spatial reticulated grid components, large deformation and stress concentration may occur in the process of mechanized installation, which will affect the assembly accuracy and installation quality of the arch. Therefore, the finite element software ABAQUS version 6.14 developed by Dassault company in France is used to test the working state of the intermediate boom when lifting the three A components at the arch crown, so as to clarify the stress and deformation laws of the key parts during the lifting process, which provides a reference for on-site mechanized construction.

4.2.1. Numerical Calculation Model

A typical double-lane underground tunnel is selected as the research background, and the spatial beam element model of the spatial reticulated grid is established, in which the number of elements is 5558 and the number of nodes is 10,435. The diameter and wall thickness of the steel tubes are 50 mm and 6 mm, respectively, and the diameter of the connecting rebar is 14 mm, which are simulated by the three-node quadratic space beam element (B32). The mechanical response of the components under the action of gravity is analyzed, the influence of the joint is not considered in the calculation, and the connection between the connecting rebar and the steel tube is simplified, to some extent. The main mechanical parameters of the steel are selected according to Table 2. According to the different snatch positions of the spatial reticulated grid, two comparative working conditions are set, which are the 1/2 position and the 1/3 position. The specific conditions are shown in Figure 17.

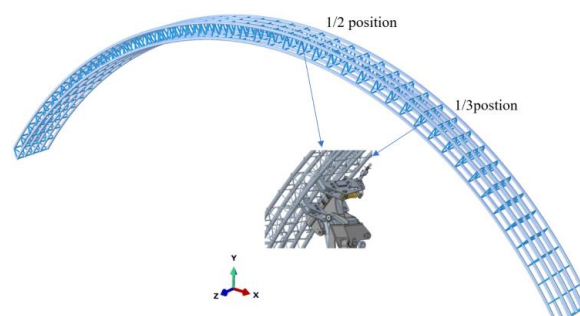


Figure 17. Calculation model of prefabricated spatial reticulated grid.

4.2.2. Analysis of the Simulation Results

(1) 1/2 position

It can be observed from Figure 18 that the maximum stress value of the spatial reticulated grid is 181.8 MPa, which occurs at the position of the vault close to the spandrel, and there is an obvious stress concentration phenomenon at the connection between the rebar and the steel tube. The closer to the two ends of the components, the smaller the stress value, the better the stress state.

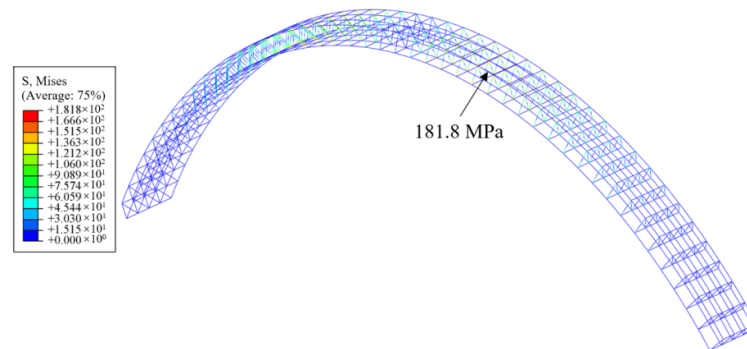


Figure 18. Mises stress nephogram of spatial reticulated grid.

It can be observed from Figure 19 that from the vault to both ends, the vertical and transverse deformation of the spatial reticulated grid gradually increases, the maximum transverse deformation is 14.15 mm, and the maximum vertical deformation is 30.27 mm. In general, all parts of the components are in good working condition, the force is reasonable, and the deformation amplitude is small, which verifies that the designed spatial reticulated grid has sufficient strength and rigidity.

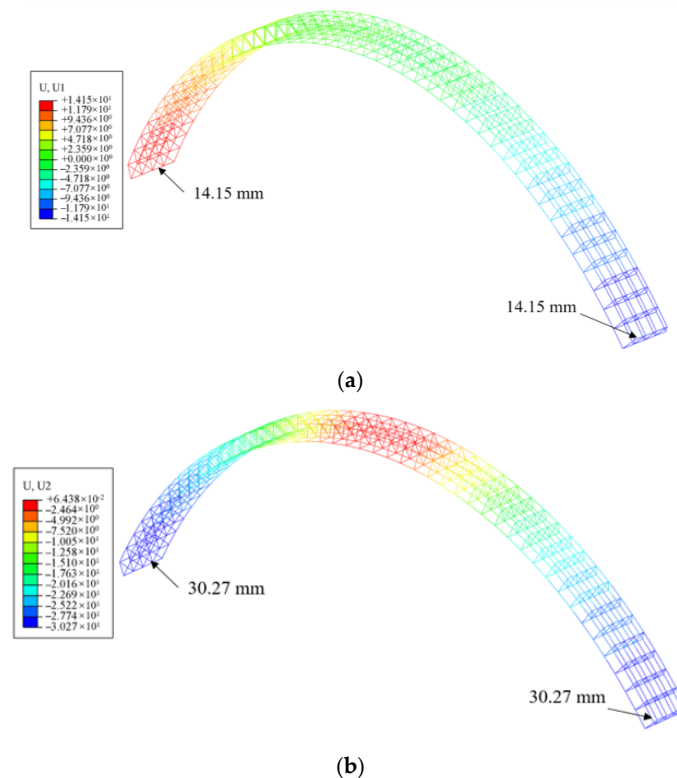


Figure 19. Deformation nephograms of the spatial reticulated grid. (a) Transverse deformation and (b) vertical deformation.

(2) 1/3 position

It can be observed from Figure 20 that the maximum stress position of the spatial reticulated grid occurs near the snatch point, with a magnitude of 446.7 MPa, which is close to the yield strength of the main limb steel tube, but exceeds the yield strength of the connecting rebar.

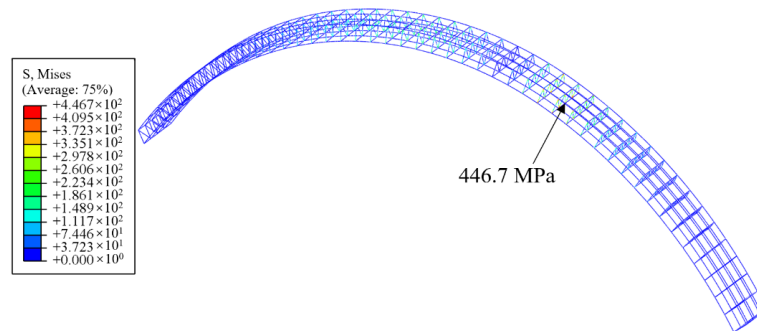


Figure 20. Mises stress nephogram of spatial reticulated grid.

It can be observed from Figure 21 that the maximum transverse and vertical deformations of the spatial reticulated grid both occur at the leftmost end, which are 77.43 mm and 213.6 mm, respectively. In summary, the selection of the snatch position has a significant impact on the deformation and force of the components. When assembling the arch, the middle position should be selected as the snatch point to minimize the adverse effect of the arch installation on the overall structural performance.

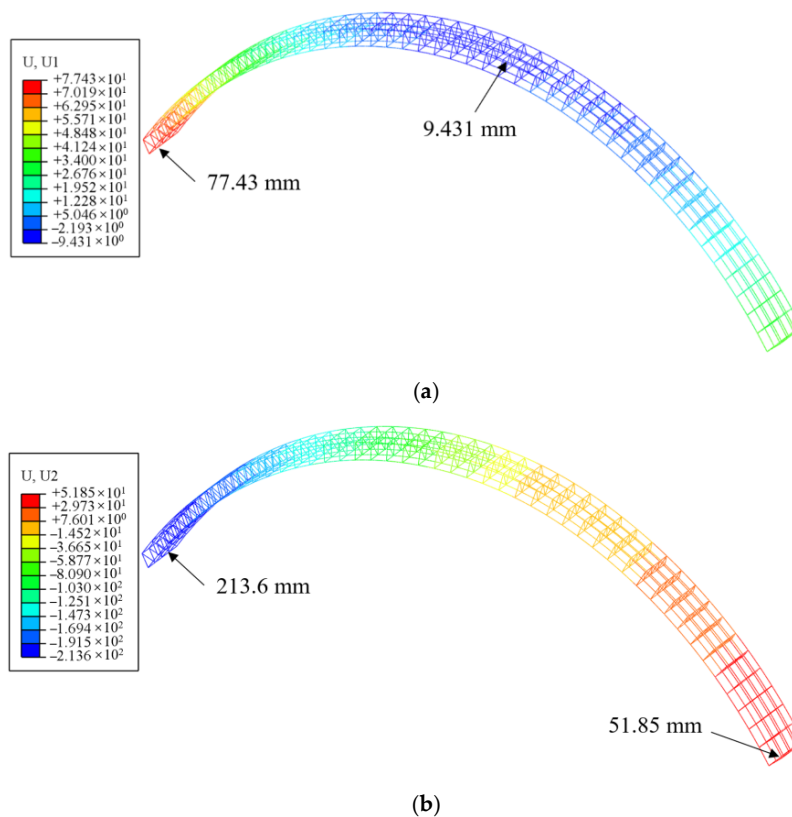


Figure 21. Deformation nephograms of the spatial reticulated grid. (a) Transverse deformation and (b) vertical deformation.

5. Field Application and Monitoring Analysis

The SRGB support structure belongs to a new type of technology and new process. In order to further clarify the adaptability and feasibility of this support structure in the subway tunnels in bustling urban areas, and to grasp the supporting working status, the field application test of the spatial reticulated grid was carried out. It highlights the performance advantages of the spatial reticulated grid, and provides a safety guarantee for the mechanized and rapid construction of urban underground space engineering.

5.1. Project View

The underground tunnel project of Panyu Square Station of Guangzhou Rail Transit Line 22 has a total length of 262.5 m, and the geographical location of the project is shown in Figure 22. The buried depth of the test tunnel is about 26.5 m, and the size of the excavation section (width \times height) is 14.9 m \times 11.95 m. The single-hole double-track horseshoe-shaped composite lining structure is adopted, the quality grade of surrounding rock is grade IV, and the bench method is adopted for construction. The minimum horizontal clear distance between the tunnel and Luojiayong bridge piles is only 2.06 m. There are many complex pipelines and major control structures, such as large hotels and libraries, on the ground. The specific location relationship is shown in Figure 23.



Figure 22. The geographical location of the underground tunnel project in the urban area in Guangzhou, China.

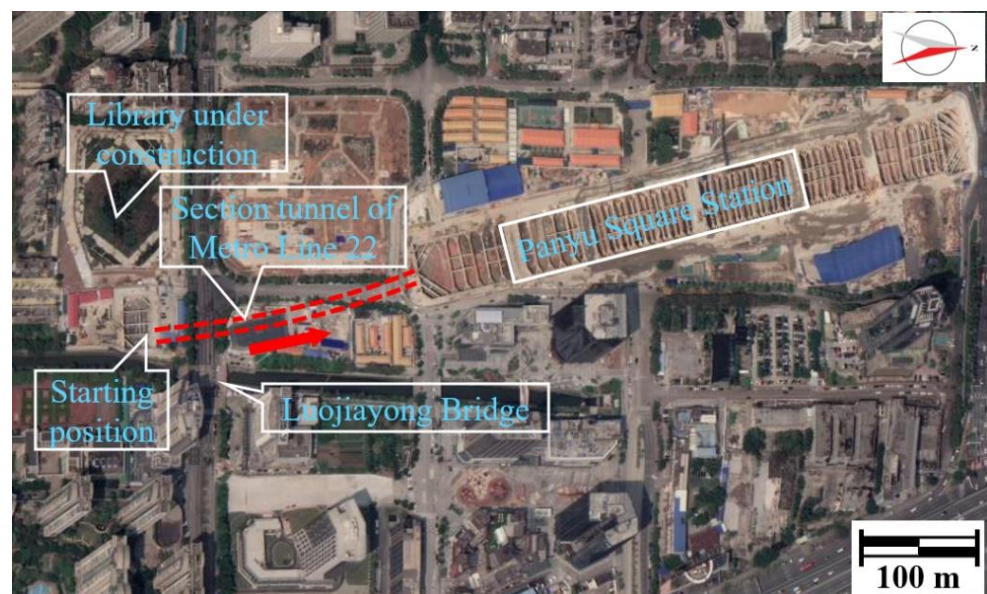


Figure 23. Surrounding environment of section tunnel project.

The design parameters of the primary support of the tunnel are as follows: the longitudinal spacing of the spatial reticulated grid is 1.0 m; and steel mesh diameter is 8 mm, with a spacing of 15 cm × 15 cm; the shotcrete grade is C25, and the thickness of the sprayed layer is 35 cm; early-strength mortar bolts diameter is 22 mm, the length is 3.0 m, and the row spacing is 1.0 m × 1.0 m. The arch foot and side wall are equipped with 42 mm diameter locking anchor tubes, and the single length is 2.0 m.

5.2. On-Site Mechanized Installation Process

(1) The preparation before construction

The staff observes whether the road surface of the tunnel meets the safe passage of the multi-functional operation trolley. If the traffic conditions are not met, the road surface needs to be repaired; one must check the overbreak and underbreak of the tunnel face, if the tunnel shows signs of underbreak, it needs to be dealt with in advance. Field processing is shown in Figure 24.



(a)



(b)

Figure 24. The preparation before construction. (a) Road surface treatment and (b) the overbreak and underbreak treatment.

(2) Mechanized installation

The erection sequence of the spatial reticulated grid is the arch top A component, the spandrel B component, the arch waist C component, the arch foot D component, and the arch bottom E component. When installing the arches on the upper bench, each of the left, middle, and right arms grab an A component for ground assembly, and at the same time, the reinforcement mesh is bound. After that, the left and right mechanical arms complete the action of releasing the arches, and the middle arm lifts the three A components to the design position. The height and position of the arch installation are based on the previous cycle arch, and there should be no misalignment. Afterwards, the left and right arms respectively grab a B component and assemble it with the A components, tighten the connecting bolts in a reasonable and orderly manner, firmly pad the arch feet, and set up locking foot anchor pipes for fixing. The on-site implementation is shown in Figure 25.



Figure 25. Mechanized installation of the arches. (a) Assembled arches near the ground and (b) the installation of upper bench arches.

When installing the lower bench arches, the left and right arms grab a C component respectively and connect it with the B component in a circumferential direction. Afterwards, the left and right arms grab a D component, respectively, the middle arm grabs the E component, and implement a temporary connection in sequence according to the execution sequence. Then, the arm manipulator is manipulated to adjust the spacing and height of the arches to complete the positioning. The on-site construction is shown in Figure 26.



Figure 26. Mechanized installation of arch waist and inverted arch. (a) Arch waist and (b) inverted arch.

(3) Other processes

When the mechanized installation of the arches is completed, the longitudinal connection was carried out in time, the remaining reinforcement mesh was laid, the system bolts and foot locking anchor tubes were set, and the shotcrete and other processes were also carried out to ensure the construction quality of the initial support.

5.3. Analysis of Engineering Application Effect

In order to test the application effect of the SRGB support structure, the stress conditions of the SRGB support structure during the construction process were monitored on site. The main test items include the settlement and convergence of surrounding rock, surrounding rock pressure, steel tube stress and concrete spray layer stress. The layout of measuring points on the test section is shown in Figure 27.

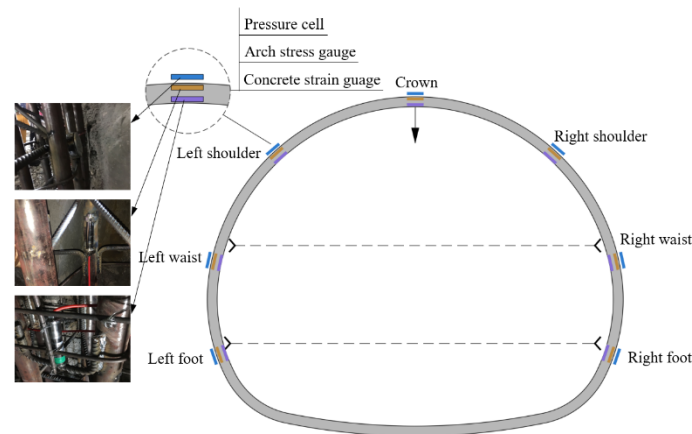


Figure 27. Schematic diagram of the layout of monitoring components.

Figure 28 shows the vault settlement and peripheral convergence duration curves of the SRG arch support section and the grid arch support section. The black line represents the grid arch support, and the red line represents the SRG arch support.

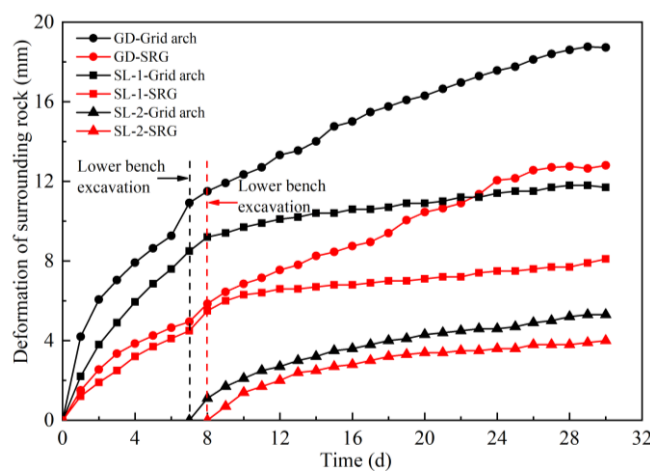


Figure 28. Duration curves of the displacement of the surrounding rock.

After nearly 30 days of real-time monitoring, the maximum settlement of the vault with the SRG arch support is 12.8 mm, which is 5.9 mm less than that with the grid arch support; in addition, the convergence deformation of the upper and lower benches is 8.1 mm and 4.0 mm, accounting for 68.6% and 75.5% of the convergence deformation of the grid arch support, respectively. The main reason is that the SRG arch has high support stiffness and bearing capacity. Under the condition of mechanized construction, it can quickly complete the accurate assembly of a heavy arch frame, close the surrounding rock in time, and effectively control the deformation after tunnel excavation.

Figure 29 shows that the distribution of the surrounding rock pressure in different positions is not the same. The contact pressure in the arch waist and arch shoulder increases more obviously, and the maximum pressure value is significantly higher than that in other positions. The pressure tends to be stable approximately six days after the excavation of the lower bench. The contact pressure of the right arch waist is the largest (244.9 kPa), followed by the left arch shoulder (124.0 kPa), left arch waist (103.5 kPa), right arch foot (70.5 kPa), vault (65.4 kPa) and left arch foot (55.8 kPa). During the whole construction process, the spatial reticulated grid structure was in the elastic deformation stage, and the stress state was good. The stress on the spandrel and the vault is generally larger, followed by the arch waist, and the arch foot is the least stressed. The concrete sprayed layer is dominated by

tensile strain, and the local position exceeds the ultimate tensile strength of concrete, but the overall structure still has high safety redundancy.

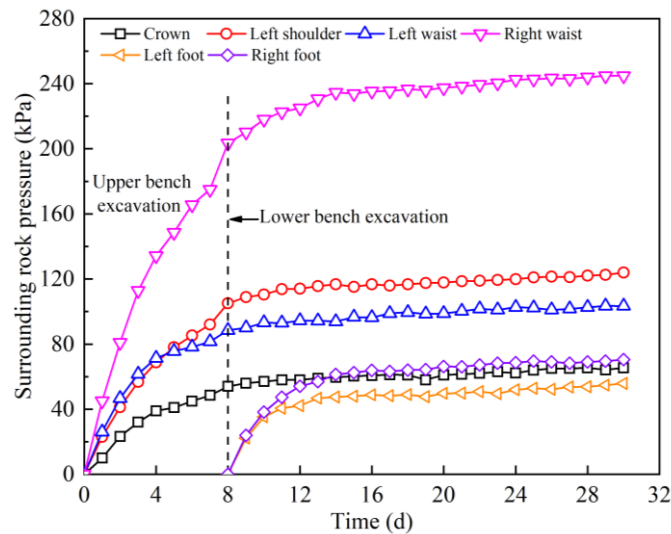


Figure 29. Duration curves of the surrounding rock pressure.

In general, by relying on the field test of the spatial reticulated grid structure carried out by the underground tunnel project of Guangzhou Metro, the first application of this structure in an urban subway tunnel has been realized. The mechanized construction method can effectively shorten the arch erection time. The high-strength, high-rigidity, and high-toughness mechanical properties of the spatial reticulated grid restrain the deformation of the surrounding rock to a great extent, and achieved good application results.

6. Conclusions

- (1) In view of the problems of high risk and strict deformation control in the construction of large cross-section underground tunnels in complex urban environments, the concept of “timely high-strength support” was put forward, in which the initial support should form strong support over time and bear the surrounding rock load in real time.
- (2) The indoor local full-scale performance tests were carried out around the concrete components with bolted end-plate joints and without joints. The failure modes and bearing characteristics of the two types of flexural components were obtained, and the law of the influence of the joint structure on the bearing performance of the components was revealed. Compared with the jointless concrete component, the bolted end-plate joint concrete component had higher flexural rigidity, and the jointless concrete component had higher ultimate bearing capacity and better deformability.
- (3) The simulation analysis of deformation and force in the snatch process of the prefabricated spatial reticulated grid was carried out, and the field test was conducted with the help of the multi-functional operation trolley, which verified the feasibility and superiority of the mechanized construction. The first successful application of the SRGB support structure in the underground tunnel of the Guangzhou metro realized the deformation control and efficient support of the large-section tunnel in the high-density area of the city, enriched the support structure system of the underground tunnel in China, and could provide a reference for similar engineering processes in the future.

Author Contributions: M.H. and Y.S.: conceptualization, methodology, project administration and writing the original draft; X.Z. and T.S.: validation, analysis, and review. All authors have read and agreed to the published version of the manuscript.

Funding: This work was supported by the General Program of National Natural Science Foundation of China (No. 51878037) and the National Key R&D Program of China (No. 2018YFC0808705).

Institutional Review Board Statement: Not applicable.

Informed Consent Statement: Not applicable.

Data Availability Statement: The data presented in this study are available upon request from the corresponding author.

Conflicts of Interest: The authors declare no conflict of interest.

References

1. Zhou, Z.; Zhang, J.J.; Gong, C.J. Automatic detection method of tunnel lining multi-defects via an enhanced You Only Look Once network. *Comput. Aided Civ. Infrastruct. Eng.* **2022**, *37*, 762–780. [[CrossRef](#)]
2. Keawsawasvong, S.; Ukritchon, B. Design equation for stability of a circular tunnel in anisotropic and heterogeneous clay. *Undergr. Space* **2022**, *7*, 76–93. [[CrossRef](#)]
3. Keawsawasvong, S.; Ukritchon, B. Design equation for stability of shallow unlined circular tunnels in Hoek-Brown rock masses. *Bull. Eng. Geol. Environ.* **2020**, *79*, 1–24. [[CrossRef](#)]
4. Sirimontree, S.; Keawsawasvong, S.; Ngamkhanong, C.; Seehavong, S.; Sangjinda, K.; Jearsiripongkul, T.; Thongchom, C.; Nuaklong, P. Neural network-based prediction model for the stability of unlined elliptical tunnels in cohesive-frictional soils. *Buildings* **2022**, *12*, 444. [[CrossRef](#)]
5. Baumann, T.; Betzle, M. Investigation of the performance of lattice girders in tunnelling. *Rock Mech. Rock Eng.* **1984**, *17*, 67–81. [[CrossRef](#)]
6. Nomikos, P.P.; Sofianos, A.I.; Sakkas, K.M.; Choumanidis, D.; Delendas, S. Nonlinear simulation of lattice girder segment tests. *Tunn. Undergr. Space Technol.* **2013**, *38*, 180–188. [[CrossRef](#)]
7. Kim, H.J.; Song, K.I.; Jung, H.S.; Shin, Y.W.; Shin, J.H. Performance evaluation of lattice girder and significance of quality control. *Tunn. Undergr. Space Technol.* **2018**, *82*, 482–492. [[CrossRef](#)]
8. Lee, J.W.; Min, K.N.; Jeong, J.W.; Roh, B.K.; Lee, S.J.; Ahn, T.B.; Kang, S.S. Development of high strength lattice girder and evaluation of its performance. *J. Eng. Geol.* **2020**, *30*, 43–57.
9. Kim, S.; Han, T.H.; Baek, J.S.; Kang, Y.J. Evaluation of the Structural Performance of Tetragonal Lattice Girders. *Int. J. Steel Struct.* **2013**, *13*, 31–47. [[CrossRef](#)]
10. Qiu, W.G.; Lu, F.; Wang, G.; Huang, G.; Zhang, H.J.; Zhang, Z.Y.; Gong, C. Evaluation of mechanical performance and optimization design for lattice girders. *Tunn. Undergr. Space Technol.* **2019**, *87*, 100–111. [[CrossRef](#)]
11. Tan, Z.S.; Han, K.H. Experimental study on the application of heat-treated high-strength lattice girder in tunnel engineering. *Symmetry* **2019**, *11*, 1007. [[CrossRef](#)]
12. Gong, C.J.; Ding, W.Q.; Mosalam, K.M.; Günay, S.; Soga, K. Comparison of the structural behavior of reinforced concrete and steel fiber reinforced concrete tunnel segmental joints. *Tunn. Undergr. Space Technol.* **2017**, *68*, 38–57. [[CrossRef](#)]
13. Ding, W.Q.; Gong, C.J.; Mosalam, K.M.; Soga, K. Development and application of the integrated sealant test apparatus for sealing gaskets in tunnel segmental joints. *Tunn. Undergr. Space Technol.* **2017**, *63*, 54–68. [[CrossRef](#)]
14. Wang, Q.; Luan, Y.C.; Jiang, B.; Li, S.C.; He, M.C.; Sun, H.B.; Qin, Q.; Lu, W. Study on key technology of tunnel fabricated arch and its mechanical mechanism in the mechanized construction. *Tunn. Undergr. Space Technol.* **2019**, *83*, 187–194. [[CrossRef](#)]
15. Wang, J.; Hu, C.C.; Zuo, J.P.; Wang, B.; Mao, Q.F.; Ding, H.G.; Zhao, N.N. Mechanism of roadway floor heave and control technology in fault fracture zone. *J. China Coal Soc.* **2019**, *44*, 397–408.
16. Song, Y.; Huang, M.L.; Zhang, X.D.; Li, Z.P.; Peng, X.X. Experimental and numerical investigation on bearing capacity of circumferential joint of new spatial steel tubular grid arch in mined tunnel. *Symmetry* **2020**, *12*, 2065. [[CrossRef](#)]
17. Huang, M.L.; Song, Y.; Zhang, X.D. Research and application of a prefabricated spatial reticulated shell support system for large cross-section tunnel in a complex urban environment. *Appl. Sci.* **2022**, *12*, 5058. [[CrossRef](#)]
18. Hisatake, M. Effects of steel fiber reinforced high-strength shotcrete in a squeezing tunnel. *Tunn. Undergr. Space Technol.* **2003**, *18*, 197–204. [[CrossRef](#)]
19. Li, Z.J.; Guo, X.X.; Ma, Z.W.; Yang, T.L.; Xu, J.Q. Research status and high-strength pre-stressed primary (type) support system for tunnels with large deformation under squeezing conditions. *Tunn. Constr.* **2020**, *40*, 755–782.
20. Luo, J.W.; Zhang, D.L.; Fang, Q.; Li, A.; Sun, Z.Y.; Cao, L.Q. Analytical study on pretensioned bolt-cable combined support of large cross-section tunnel. *Sci. China Technol. Sci.* **2020**, *63*, 1808–1823. [[CrossRef](#)]
21. Sun, J.; Jiang, Y.; Wang, B.; Fan, Y. Nonlinear rheological properties and yielding support technology for large squeezing deformation of soft rock tunnel with high ground stress. *Tunn. Constr.* **2021**, *41*, 1627–1633.
22. Wu, K.; Shao, Z.S.; Qin, S.; Wei, W.; Chu, Z.F. A critical review on the performance of yielding supports in squeezing tunnels. *Tunn. Undergr. Space Technol.* **2021**, *115*, 103815. [[CrossRef](#)]
23. Kong, X.Y.; Chen, X.; Tang, C.A.; Sun, Z.R.; Hu, E.H. Study on large deformation control technology and engineering application of tunnel with high ground stress and weak broken surrounding rock. *Struct. Eng. Int.* **2020**, *32*, 1–9. [[CrossRef](#)]

24. He, M.C.; Gong, W.L.; Wang, J.; Qi, P.; Tao, Z.G.; Du, S.; Peng, Y.Y. Development of a novel energy-absorbing bolt with extraordinarily large elongation and constant resistance. *Int. J. Rock Mech. Min. Sci.* **2014**, *67*, 29–42. [[CrossRef](#)]
25. Zheng, Y.T.; Zhu, S.Y.; Li, S.L.; Song, R.C.; Guo, T. Testing research on a composite support system using bolts, shotcrete, mesh and arc plates for a tunnel in soft rock mass. *Chin. J. Rock Mech. Eng.* **1993**, *12*, 3–12.
26. Chang, Q.L.; Zhou, H.Q.; Li, D.W.; Bai, J.B.; Hou, C.J. Stability Principle of Extremely Rigid Secondary Support for Soft and Broken Rock Roadway. *J. Min. Saf. Eng.* **2007**, *24*, 169–172+177.
27. Liu, D.J.; Zuo, J.P.; Wang, J.; Zhang, T.L.; Liu, H.Y. Large deformation mechanism and concrete-filled steel tubular support control technology of soft rock roadway-A case study. *Eng. Fail. Anal.* **2020**, *116*, 104721. [[CrossRef](#)]
28. Huang, W.P.; Yuan, Q.; Tan, Y.L.; Wang, J.; Liu, G.L.; Qu, G.L.; Li, C. An innovative support technology employing a concrete-filled steel tubular structure for a 1000-m-deep roadway in a high in situ stress field. *Tunn. Undergr. Space Technol.* **2018**, *73*, 26–36. [[CrossRef](#)]
29. Wang, Z.C.; Du, K.; Xie, Y.L.; Su, X.L.; Shi, Y.F.; Li, X.; Liu, T. Buckling analysis of an innovative type of steel-concrete composite support in tunnels. *J. Constr. Steel Res.* **2021**, *179*, 106503. [[CrossRef](#)]
30. Xu, F.; Li, S.C.; Zhang, Q.Q.; Li, L.P.; Shi, S.S.; Zhang, Q. A new type support structure introduction and its contrast study with traditional support structure used in tunnel construction. *Tunn. Undergr. Space Technol.* **2016**, *63*, 171–182. [[CrossRef](#)]
31. Yao, W.J.; Pang, J.Y.; Zhang, J.S.; Liu, G.C. Key technique study of stability control of surrounding rock in deep chamber with large cross-section: A case study of the Zhangji coal mine in China. *Geotech. Geol. Eng.* **2020**, *39*, 299–316. [[CrossRef](#)]
32. Li, C.; Wang, Z.L.; Liu, T. Principle and practice of coupling support of double yielding shell of soft rock roadway under high stress. *Int. J. Min. Sci. Technol.* **2014**, *24*, 513–518. [[CrossRef](#)]
33. *TB-10003*; Code for Design of Railway Tunnel. China Railway Publishing House: Beijing, China, 2016.